Numerical comparison of a tidal turbine using three methods to characterize the blade rotation

Journal of Physics: Conference Series **3224** (2026) 032063 doi:10.1088/1742-6596/3224/3/032063

Numerical comparison of a tidal turbine using three methods to characterize the blade rotation

Linyang Zhu[1,2*], Himpu Marbona[1], Oscar A Marino[1], Esteban Ferrer[1]

[1] School of Aeronautical and Space Engineering, Universidad Politécnica de Madrid, Madrid, Spain
2 School of Mechanics and Aerospace Engineering, Southwest Jiaotong University, Chengdu 611756, China

[*]E-mail: linyang.zhu@upm.es

Quantifying the discrepancies introduced by different rotor modelling approaches is essential for understanding their predictive capability and limitations. This study presents numerical simulations (using ANSYS Fluent and HORSES3D[1]) of a horizontal-axis tidal turbine with 1.6 m diameter rotor under design operating conditions, where the tip speed ratio is set to be 6.03. The multi reference frame, sliding mesh and actuator line techniques are used to simulate the rotation. The predicted force coefficients and moment coefficients are validated by comparison with experimental data, which is from the Tidal Turbine Benchmarking Project conducted and funded by the UK's EPSRC and Supergen ORE Hub[2]. It is shown that the force coefficients predicted using the sliding mesh technique are closer to the experimental data while the actuator line method predicts the bending moment coefficients more accurately. Overall, the actuator line method coupling with large eddy simulation in HORSES3D performs an encouraging accuracy for the turbine performance and demonstrates its advantage over Reynolds-averaged Navier–Stokes (RANS) equations for the downstream wake structures.

1. Introduction

Global climate change and the associated rise in greenhouse gas emissions have intensified the urgent need for the development and deployment of renewable energy technologies. Among various alternatives, tidal energy has attracted considerable attention due to its predictability, stability, and vast potential for sustainable electricity generation. By harnessing the kinetic energy of tidal currents, turbines can be employed to convert hydrodynamic forces into mechanical rotation and subsequently into electrical power. To ensure the viability and large-scale deployment of tidal turbine systems, accurate performance assessment of the turbine is of fundamental importance.

In the context of numerical modelling, a range of computational approaches have been developed to represent the rotor–fluid interactions at different levels of fidelity and computational cost. Simplified approaches such as the blade element momentum (BEM) method provide efficient performance predictions but rely heavily on empirical corrections and assumptions regarding wake development. More advanced techniques include the actuator line method (AL), which distributes blade forces along rotating lines to capture unsteady wake dynamics with moderate computational demand, and fully blade-resolved simulations, which

explicitly model the rotating turbine blades and resolve the detailed flow features but requiring higher computational cost.

Baratchi et al. [3] simulated tidal turbines using the AL method for several tip speed ratios and compared with the results from the blade element actuator disk (BEAD) method. Mohamed et al. [4] assessed the influence of the input polars, the dynamic stall modelling, and the location of the force in the results' accuracy when applying the AL method to vertical-axis turbines. Baba-Ahmadi et al. [5] used AL to simulate wake characteristics. Engineering-oriented computational fluid mechanics (CFD) approaches such as the multiple reference frame (MRF) method and the sliding mesh technique have been widely adopted in turbomachinery studies. The MRF method approximates steady-state rotor–fluid interactions by imposing a rotating reference frame, thereby reducing computational requirements while capturing averaged flow features. The sliding mesh approach, on the other hand, accounts for the relative motion between the rotor and the surrounding fluid through dynamic mesh interfaces, enabling transient wake prediction and providing a more accurate representation of unsteady phenomena such as vortex shedding and periodic flow structures at the expense of higher computational cost. Generally, the sliding mesh method is used based on the initial solution by the MRF method. These methods have also been widely adopted for simulating turbines. For example, Ahmed et al. [6] investigated the fluctuating loads on the tidal turbine coupling with large eddy simulation (LES). Mo et al. [7] used sliding meshes to conduct wake characterization of the wind turbine. Additional relevant work includes [8], [9], [10], [11]. From this review, it can be concluded that these approaches, together with the actuator line method, provide a range of modelling strategies that balance efficiency and accuracy in turbine performance prediction.

To advance the understanding of tidal turbine modelling, the present study systematically compares the actuator line method, the MRF method and the sliding mesh method in simulating the laboratory-scale tidal turbine model under the design condition at a tip speed ratio $\lambda = 6.03$ which is defined as

$$\lambda = \frac{\Omega R}{U_\infty} \tag{1}$$

where Ω, R and U_∞ denote the rotation angular velocity, radius and incoming flow velocity respectively. The first method was implemented using an open-source high-order solver HORSES3D, while the rest two methods were conducted using ANSYS Fluent 2022 R1, which is a general commercial CFD solver. By benchmarking these numerical strategies against a well-documented experimental case, this work aims to assess and compare their predictive capabilities.

2. Methods

For the AL method, each blade is simplified as an actuator line distributed along the radial direction, where the local forces are determined based on the incoming flow velocity, angle of attack (AOA) and the corresponding lift and drag coefficients. These forces are then projected to the flow field as body force source terms, typically smoothed by the following Gaussian distribution to ensure numerical stability,

$$G(d) = \frac{1}{\varepsilon^3 \pi^{3/2}} e^{-(d/\varepsilon)^2} \tag{2}$$

where d is the distance between the actuator point and the grid node and ε is the width of the projection. In this work, the actuator line is uniformly divided to 37 sections, which falls within

the range of 30 to 60 reported by Baratchi et al[3]. The Gaussian projection factor is set as $\varepsilon / \Delta = 2.5$, where Δ is the local grid cell size. The value of ε/Δ is close to 2 which is recommended by Troldborg and has been adopted in many works[3], [12], [13]. Too small value can lead to numerical instability, whereas an overly large value compromises actuator-line representation accuracy of the blades. Besides, the tip loss correction is achieved using the Shen et al. model[14]. The point forces used for the AL are imposed at the high-order Gauss-Lobatto points. In HORSES3D, we run the compressible Navier-Stokes equations (at low Mach to mimic the incompressible limit). The LES subgrid-scale stresses are calculated using the Vreman eddy-viscosity model. Viscous terms are discretized using the BR1 (Bassi–Rebay 1) scheme, while a Lax–Friedrichs Riemann solver is employed for interface flux evaluation. The inviscid fluxes are computed using a Kennedy–Gruber split-form formulation to improve energy stability. An explicit scheme is employed for time discretization, and the Courant–Friedrichs–Lewy (CFL) number is fixed at 0.6 throughout the simulations. The AL method coupling with LES is implemented in the high-order discontinuous Galerkin HORSES3D, which has been widely used to the turbine simulations such as [15], [16], [17] et al.

For the two blade-resolved methods in ANSYS-Fluent, the governing discretized differential equations are solved using the pressure-based solver. The pressure–velocity coupling is achieved by the SIMPLE algorithm. Spatial gradients are calculated using a least-squares cell-based method, and a second-order upwind scheme is adopted for the discretization of the convective terms. The turbulent eddy viscosity is computed using the $k-\omega$ shear stress transport (SST) model. The simulations are first conducted with steady-state Reynolds-averaged Navier–Stokes (RANS) equations using the MRF method, which is iterated until the differences of the thrust coefficient and power coefficient between successive iterations fall below 10^{-7}. The sliding mesh method uses the MRF simulation as initial condition, which is switched to the unsteady solver (URANS) for the sliding part. A time step size of 0.002 s is employed referring to Mo et al. [7], corresponding to a blade rotation of less than 1° per time step.

3. Case description

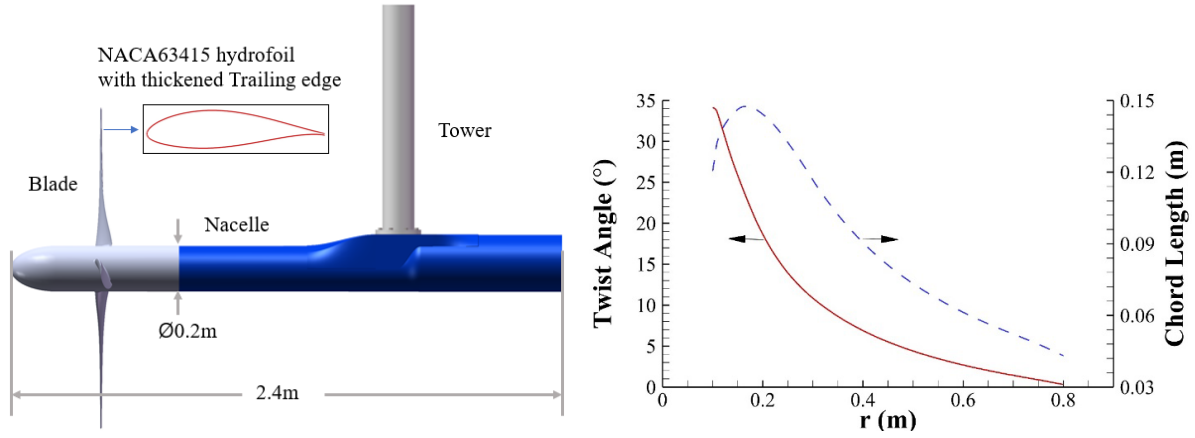

(a) geometry model (b) blade parameters

Figure 1. Geometry description of the turbine.

The turbine geometry is from the Tidal Turbine Benchmarking Project [15],[16]. The experiments were conducted in a towing tank with a width of 12.2 m and a depth of 5.4 m,

corresponding to a blockage ratio of 3.05%. The rotor consists of three blades with a rotational radius of 0.8 m, while the nacelle has a diameter of 0.2 m and a length of 2.4 m. The turbine model is supported by the upper tower to move in the experiment tank. The NACA 63415 hydrofoil profile with thickened trailing edge was selected for the blades to be consistent with the experimental model. In the numerical simulation, small components such as bolts and flanges were neglected for simplification. A schematic representation is provided in Figure 1(a) and the blade parameters are shown in Figure 1(b). More information about the geometry is detailed in [2]. The provided polar curve of the NACA 63415 hydrofoil for nearly zero turbulence intensity is used throughout for the AL method, which is shown in Figure 2 for both lift coefficient C_l and drag coefficient C_d.

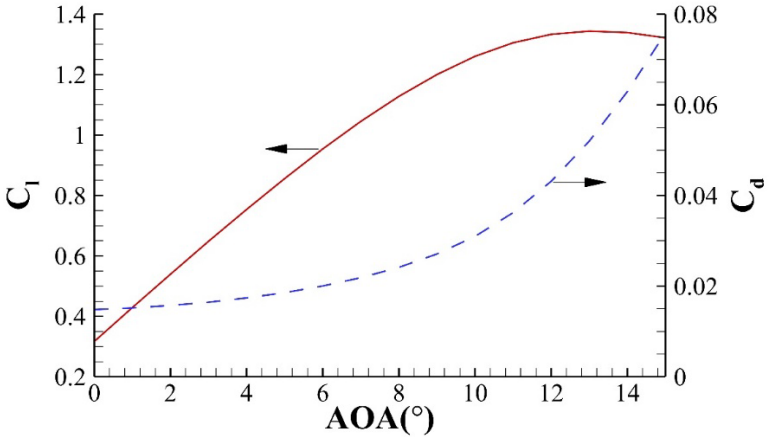

Figure 2. Polar curve of the NACA 63415 hydrofoil

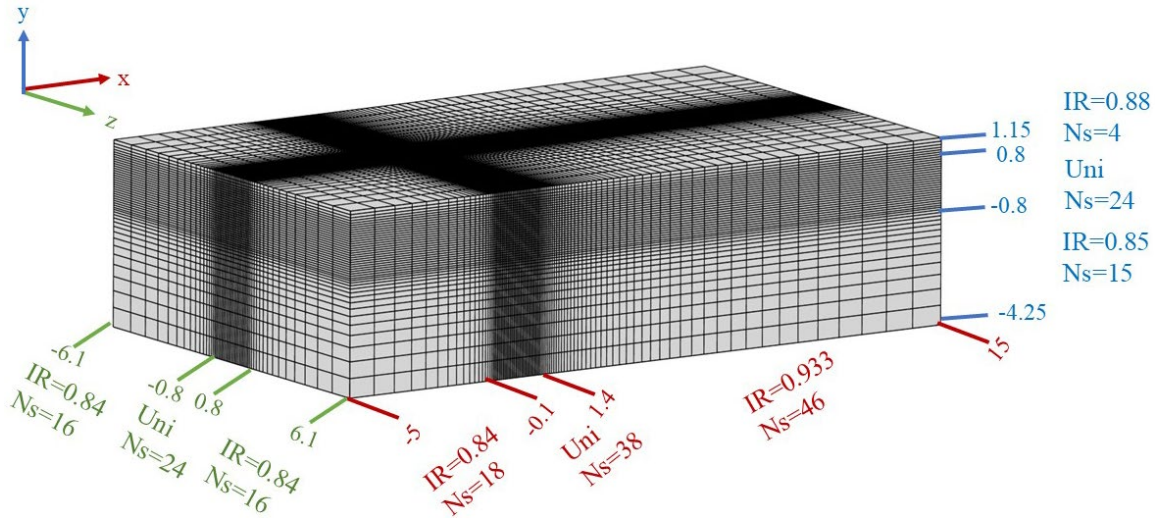

Figure 3. Structured Cartesian mesh for the AL method

The structured Cartesian mesh was used for the AL method. The domain size is the same as the experimental tank as shown in Figure 3. In this figure, the red, blue and green are marks and notes for the x, y and z axis respectively, where the number indicates the coordinate and *Uni* means the nodes are uniformly distributed. *IR* is the increasing ratio, and *Ns* is the node number. The rotating region containing the geometric model was locally refined for better resolution, viz

$x \in [-0.1, 1.4]$, $y \in [-0.8, 0.8]$, $z \in [-0.8, 0.8]$. The left and right surface were specified as inflow and outflow boundary conditions, respectively, while the remaining side surfaces were treated as free-slip walls. Along the blade span, 12 nodes were distributed. Considering that a polynomial order $P = 3$ was employed, the corresponding degree of freedom (DOF) for each actuator line is 48, which satisfies the resolution recommended in the literature [12]. The final mesh includes 258324 nodes and 245616 cells, which leads to 16532736 degrees of freedom for $P = 3$. The nacelle and tower are modelled with the immersed boundary method.

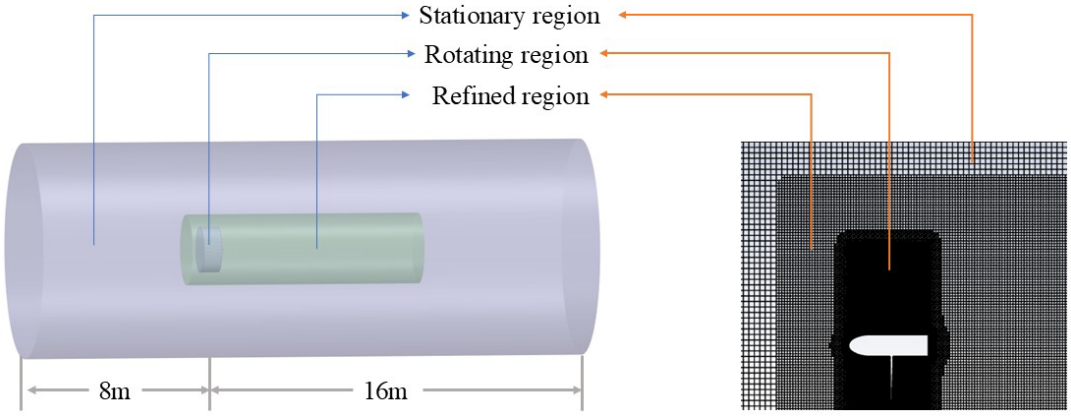

Figure 4. Computation domain and the corresponding local mesh

Table 1. Computation domain size for the blade-resolved methods

Size(m)	Rotating region	Stationary region	Refine region
Length	0.774	24	10
Diameter	1.92	9.16	3

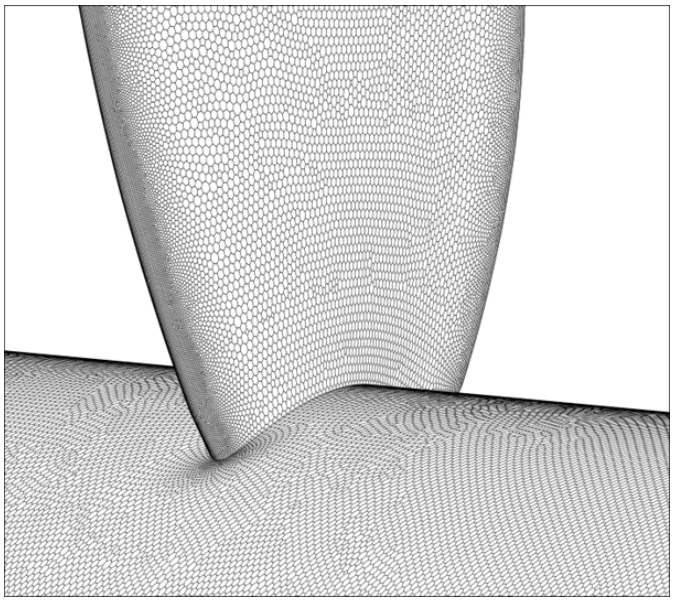

Figure 5. Local mesh at the junction of blade and nacelle

The poly-hexcone hybrid mesh was used for the blade-resolved methods, which combines a high-quality hexahedral core with polyhedral transitions and provides accurate resolution in critical regions while adapting to complex geometries. This topology improves numerical stability and efficiently captures boundary layers and wake flows. We performed a preliminary mesh convergence (not shown) and proceed with the retained mesh to compare favourably with experimental values. The domain includes three regions, where the refined region was used to resolve more wake details with refined mesh (see Figure 4). All the regions are cylinders with the size detailed in Table 1. The left and right surfaces of the stationary region were set as velocity-inlet and pressure-outlet boundary conditions respectively, while the lateral surface was set as slip wall. The sliding surfaces were treated as the interface and the non-slip wall was implemented on the blades and nacelle. The mesh was clustered in the leading and trailing edge of the blade to resolve the geometry (see Figure 5). The height of the first layer at the wall was set to be 4×10^{-6} m to satisfy $y^+<1$, which is shown in Figure 6. Such a mesh includes 38626098 cells, of which 21823885 is in the rotating region. Note that the tower is not included in the ANSYS-Fluent simulations (blade-resolved methods).

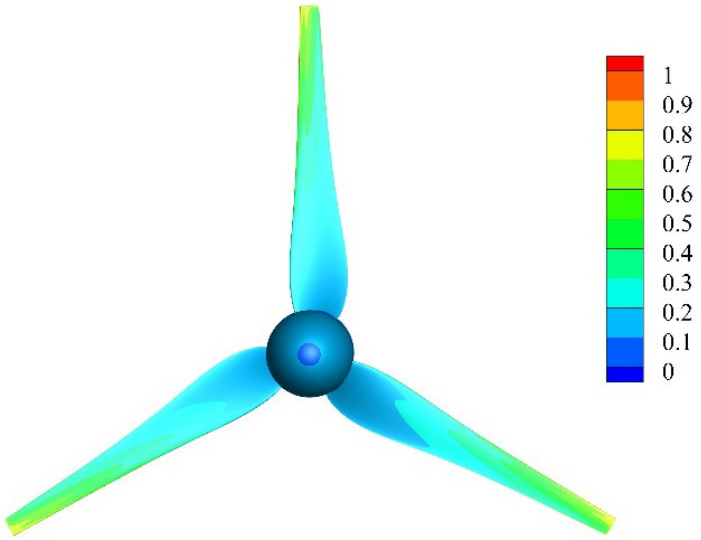

Figure 6. y^+ contour at the wall

4. Result and discussion

In this section, the primary focus is placed on the power coefficient C_P and thrust coefficient C_T which are define as

$$C_P = \frac{P}{1/2\rho U_\infty^3 \pi R^2} \tag{3}$$

$$C_T = \frac{T}{1/2\rho U_\infty^2 \pi R^2} \tag{4}$$

where ρ is the fluid density, P and T denoting the rotor power and thrust respectively. The experimental results are taken from [2] which include some uncertainty. The experimental values presented in Table 1 correspond to conditions with low turbulence intensity. It should be noted

that the numerical simulations assume fully turbulent inflow without accounting for laminar-to-turbulent transition on the blades.

Table 2 presents a comparison of the power coefficient and thrust coefficient obtained from experiments and three numerical approaches. For the power coefficient, the AL method overpredicts the experimental result by approximately 6.9%. In comparison, the MRF method shows a better agreement with the experimental data with about 1.5% discrepancy. For the thrust coefficient, the predicted value of the AL method is 0.855, which is nearly 2.2% lower than the experimental result, whereas MRF generates a 0.5% overprediction. Noticeably, both the power coefficient and thrust coefficient predicted by the sliding mesh collapse excellently with the experimental data. Overall, MRF and sliding mesh demonstrates a very good agreement for both power and thrust coefficients, while the AL method shows a slightly larger discrepancy.

Table 2. Comparison of power coefficient and thrust coefficient

Coefficient	Experiment	AL	MRF	Sliding mesh
C_P	**0.478**	0.511	0.485	0.478
C_T	**0.874**	0.855	0.878	0.875

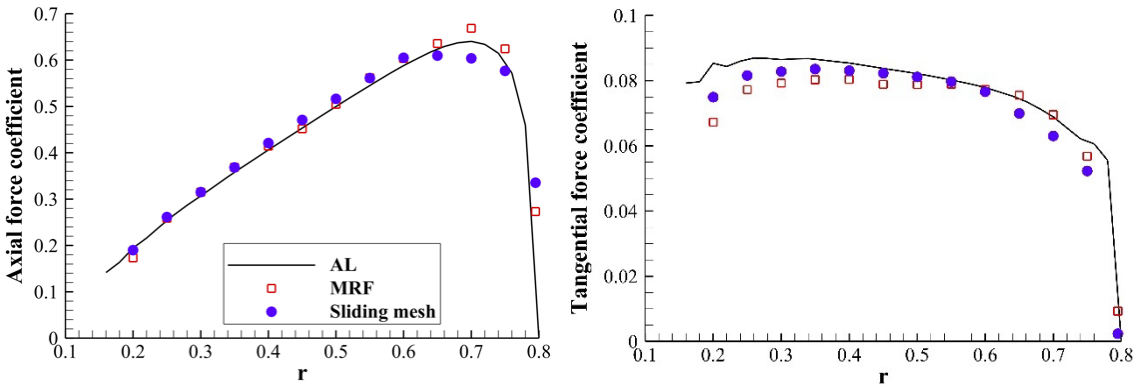

(a) Axial direction (b) Tangential direction

Figure 7. Force coefficients along the blade

Figure 7 shows the radial distribution of the force coefficients, where r denotes the distance to the rotation axis. To obtain the force coefficients along the blade from the blade-resolved simulations, 13 sections were extracted at intervals of 0.05m within the radial range [0.2, 0.8]. For convenience of comparison, the forces were calculated per unit radial length and non-dimensionalized in the same way as the thrust (see eq. (4)). The AL method underpredicts the axial (thrust) force coefficient over most of the blade span while overpredicts the tangential force coefficient. This result is consistent with the deviations observed in Table 2 for the power and thrust coefficients. Larger discrepancies are observed near the blade root and tip, which can be to some extent attributed to the limitations of the tip loss correction employed in the AL method to characterize the complex flows.

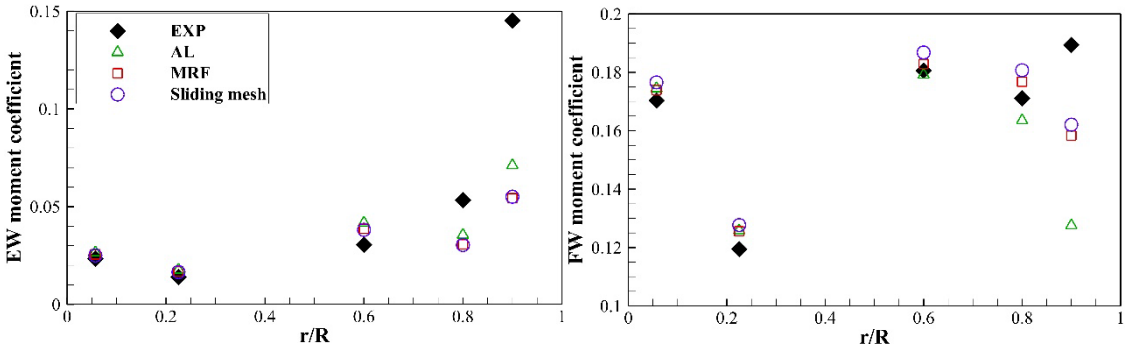

(a) Edgewise direction (b) Flapwise direction

Figure 8. Bending moment coefficients along the blade

Figure 8 shows the comparison of the bending moment coefficients along the blade, which is defined as

$$C_M = \frac{M}{1/2\rho U_\infty^2 \pi R^3}, \tag{5}$$

where M is the bending moment. The specific locations r/R are 0.057, 0.225, 0.6, 0.8, 0.9, respectively. It should be noted that the edgewise (EW) bending moment coefficients of the three locations near the blade tip are amplified through multiplying factors of 10, 40 and 400 respectively to present the results in one figure clearly. Similarly, the corresponding factors for the flapwise (FW) bending moment coefficients are 5, 20 and 80 respectively.

The simulations generate the excellent prediction over the edgewise bending moment at locations $r/R < 0.8$, however, overpredict the edgewise bending moments obviously for the locations $r/R \geq 0.8$ comparing with the experimental data, which is shown is Figure 8(a). Such discrepancy is actually similar with the published simulation results [18], which can be caused by the blade twist in the experiment as indicated by the experiment conductors Harvey et al. [2]. The AL method also shows an encouraging prediction over the flapwise bending moment at locations $r/R \leq 0.8$, which is comparable to the blade-resolved methods.

Figure 9 presents iso-surfaces of the Q-criterion for the turbine wake coloured by the velocity magnitude. The definition of Q can be expressed as

$$Q = \frac{1}{2}(\|\mathbf{W}\|^2 - \|\mathbf{S}\|^2) \tag{6}$$

where $\|\mathbf{W}\|$ and $\|\mathbf{S}\|$ denote the module of the rotation rate tensor and strain rate tensor respectively. Figure 9(a) shows the result from LES coupling with AL method while Figure 9(b) corresponds to that from URANS coupling with sliding mesh method. The Q-criterion is employed to identify coherent vortex structures, where positive Q values indicate regions in which the local rotation rate dominates over the strain rate. The iso-surfaces clearly reveal the development and evolution of blade-tip vortices and the helical wake structure downstream of the turbine. Colouring by the velocity magnitude highlights the strong velocity deficit within the wake core and the gradual recovery of the flow downstream. As the vortices move downstream, the strength progressively diminishes and blade-tip vortex profile becomes unclear and breaks to small eddies (see Figure 9(a)), indicating enhanced turbulent mixing and energy dissipation (probably due to the presence of the tower in the AL simulations), which contributes to the recovery of the velocity deficit in the far wake. The tower blockage and upper boundary constraint contribute to the breakdown of the blade-tip vortices. In comparison, although the mesh resolution is finer than

that in the LES, the URANS framework relies on turbulence modelling to represent unresolved fluctuations, which increases effective dissipation and accelerates vortex diffusion. Consequently, the wake appears smoother with small eddies rarely resolved, and the helical vortices exhibit merging and loss of coherence compared to the LES results (see Figure 9(b)), which indicates the advantage of the high-order spectral method in HORSES3D.

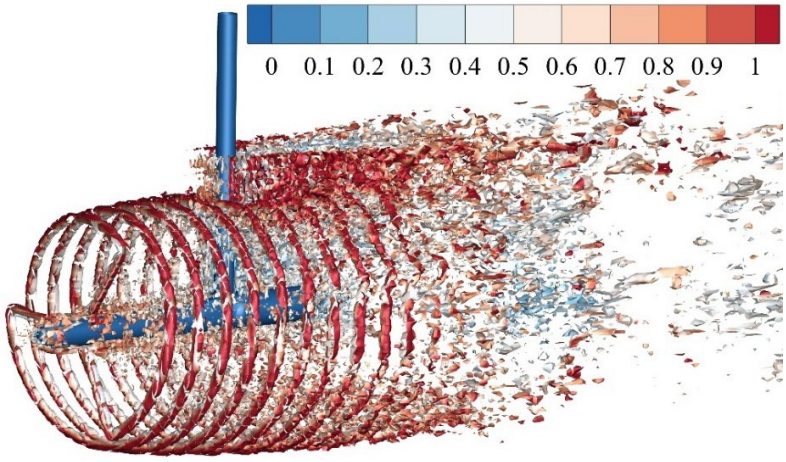

(a) LES

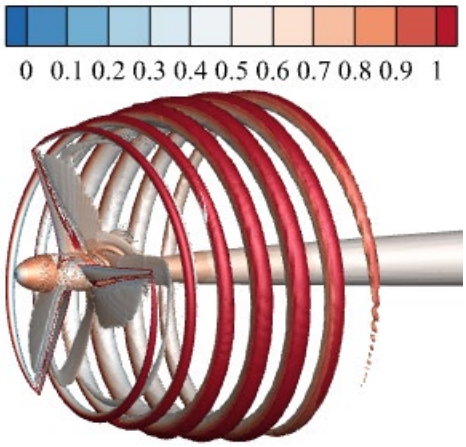

(b) URANS

Figure 9. Q-criterion iso-surfaces of 0.5 colored by the velocity magnitude

5. Conclusion

This study presents the numerical simulation results of a horizontal-axis tidal turbine benchmark case operated at the design tip speed ratio. Three numerical approaches are employed. The first is a large eddy simulation coupled with the AL method implemented in the open-source high-order spectral solver HORSES3D. The second is steady RANS simulation coupled with the MRF method and the last is URANS simulation coupled with the sliding mesh method.

The numerical results are validated against the available experimental data. The bending moment coefficients predicted by the AL method at different radial blade locations show encouraging agreement with the measurements, while the discrepancies observed in the thrust and power coefficients are acceptable. The differences in the force coefficients predicted by the AL and blade-resolved methods are mainly concentrated near the blade–nacelle junction and the

blade tip, where the AL method has limited capability to characterize the local complex flows. Furthermore, despite employing a mesh with fewer cells and degrees of freedom, the LES coupling with AL method provides a more detailed representation of the wake evolution and downstream vortex structures. This clearly demonstrates the strength of the high-order numerical scheme in resolving coherent wake dynamics.

Acknowledgements

Fundings to support this research are provided by the Marie Skłodowska-Curie Postdoctoral Fellowship (NO. 101149790) and the National Natural Science Foundation of China (No. 12202470).

This research has received funding from the European Union (ERC, Off-coustics, project number 101086075). Views and opinions expressed are, however, those of the authors only and do not necessarily reflect those of the European Union or the European Research Council. Neither the European Union nor the granting authority can be held responsible for them.

References

[1] E. Ferrer *et al.*, "A high-order discontinuous Galerkin solver for flow simulations and multi-physics applications," *Computer Physics Communications*, vol. 287, p. 108700, Jun. 2023, doi: 10.1016/j.cpc.2023.108700.

[2] S. W. Tucker Harvey *et al.*, "Tidal Turbine Benchmarking Project: Stage I - Steady Flow Experiments," *Proc. EWTEC*, vol. 15, Sep. 2023, doi: 10.36688/ewtec-2023-553.

[3] F. Baratchi, T. L. Jeans, and A. G. Gerber, "Actuator line simulation of a tidal turbine in straight and yawed flows," *International Journal of Marine Energy*, vol. 19, pp. 235–255, Sep. 2017, doi: 10.1016/j.ijome.2017.08.003.

[4] O. S. Mohamed, P. F. Melani, F. Balduzzi, G. Ferrara, and A. Bianchini, "An insight on the key factors influencing the accuracy of the actuator line method for use in vertical-axis turbines: Limitations and open challenges," *Energy Conversion and Management*, vol. 270, p. 116249, Oct. 2022, doi: 10.1016/j.enconman.2022.116249.

[5] M. H. Baba-Ahmadi and P. Dong, "Numerical simulations of wake characteristics of a horizontal axis tidal stream turbine using actuator line model," *Renewable Energy*, vol. 113, pp. 669–678, Dec. 2017, doi: 10.1016/j.renene.2017.06.035.

[6] U. Ahmed, D. D. Apsley, I. Afgan, T. Stallard, and P. K. Stansby, "Fluctuating loads on a tidal turbine due to velocity shear and turbulence: Comparison of CFD with field data," *Renewable Energy*, vol. 112, pp. 235–246, Nov. 2017, doi: 10.1016/j.renene.2017.05.048.

[7] J.-O. Mo, A. Choudhry, M. Arjomandi, and Y.-H. Lee, "Large eddy simulation of the wind turbine wake characteristics in the numerical wind tunnel model," *Journal of Wind Engineering and Industrial Aerodynamics*, vol. 112, pp. 11–24, Jan. 2013, doi: 10.1016/j.jweia.2012.09.002.

[8] F. De Girolamo *et al.*, "Detached eddy simulation of large scale wind turbine wake in offshore environment," *International Journal of Heat and Fluid Flow*, vol. 110, p. 109637, Dec. 2024, doi: 10.1016/j.ijheatfluidflow.2024.109637.

[9] M. Faizan, S. Badshah, M. Badshah, and B. A. Haider, "Performance and wake analysis of horizontal axis tidal current turbine using Improved Delayed Detached Eddy Simulation," *Renewable Energy*, vol. 184, pp. 740–752, Jan. 2022, doi: 10.1016/j.renene.2021.11.107.

[10] I. Afgan, J. McNaughton, S. Rolfo, D. D. Apsley, T. Stallard, and P. Stansby, "Turbulent flow and loading on a tidal stream turbine by LES and RANS," *International Journal of Heat and Fluid Flow*, vol. 43, pp. 96–108, Oct. 2013, doi: 10.1016/j.ijheatfluidflow.2013.03.010.
[11] P. Ouro, H. Mullings, A. Christou, S. Draycott, and T. Stallard, "Wake characteristics behind a tidal turbine with surface waves in turbulent flow analyzed with large-eddy simulation," *Phys. Rev. Fluids*, vol. 9, no. 3, p. 034608, Mar. 2024, doi: 10.1103/PhysRevFluids.9.034608.
[12] P. K. Jha, M. J. Churchfield, P. J. Moriarty, and S. Schmitz, "Guidelines for Volume Force Distributions Within Actuator Line Modeling of Wind Turbines on Large-Eddy Simulation-Type Grids," *Journal of Solar Energy Engineering*, vol. 136, no. 3, p. 031003, Aug. 2014, doi: 10.1115/1.4026252.
[13] M. J. Churchfield, S. Lee, and J. Michalakes, "A numerical study of the effects of atmospheric and wake turbine dynamics," *J Turbul.*, vol. 13, Jan. 2012.
[14] W. Z. Shen, R. Mikkelsen, J. N. Sørensen, and C. Bak, "Tip loss corrections for wind turbine computations," *Wind Energy*, vol. 8, no. 4, pp. 457–475, 2005, doi: 10.1002/we.153.
[15] L. Botero-Bolívar, O. A. Marino, C. H. Venner, L. D. De Santana, and E. Ferrer, "Low-cost wind turbine aeroacoustic predictions using actuator lines," *Renewable Energy*, vol. 227, p. 120476, Jun. 2024, doi: 10.1016/j.renene.2024.120476.
[16] H. Kessasra, M. Cordero-Gracia, M. Gómez, E. Valero, G. Rubio, and E. Ferrer, "A comparison of h- and p-refinement to capture wind turbine wakes," *Physics of Fluids*, vol. 36, no. 12, p. 125125, Dec. 2024, doi: 10.1063/5.0241311.
[17] E. Ferrer and R. H. J. Willden, "Blade–wake interactions in cross-flow turbines," *International Journal of Marine Energy*, vol. 11, pp. 71–83, Sep. 2015, doi: 10.1016/j.ijome.2015.06.001.
[18] R. H. J. Willden *et al.*, "Tidal Turbine Benchmarking Project: Stage I - Steady Flow Blind Predictions," *Proc. EWTEC*, vol. 15, Sep. 2023, doi: 10.36688/ewtec-2023-574.